

Improving needle visibility in LED-based photoacoustic imaging using deep learning with semi-synthetic datasets

Mengjie Shi, Tianrui Zhao, Simeon J. West, Adrien E. Desjardins, Tom Vercauteren and Wenfeng Xia

arXiv:2111.07673v1 [eess.IV] 15 Nov 2021

Abstract—Photoacoustic imaging has shown great potential for guiding minimally invasive procedures by accurate identification of critical tissue targets and invasive medical devices (such as metallic needles). Recently, the use of light emitting diodes (LEDs) as the excitation light sources further accelerates its clinical translation owing to its high affordability and portability. However, needle visibility in LED-based photoacoustic imaging is compromised primarily due to its low optical fluence. In this work, we propose a deep learning framework based on a modified U-Net to improve the visibility of clinical metallic needles with a LED-based photoacoustic and ultrasound imaging system. This framework included the generation of semi-synthetic training datasets combining both simulated data to represent features from the needles and *in vivo* measurements for tissue background. Evaluation of the trained neural network was performed with needle insertions into a blood-vessel-mimicking phantom, pork joint tissue *ex vivo* and measurements on human volunteers. This deep learning-based framework substantially improved the needle visibility in photoacoustic imaging *in vivo* compared to conventional reconstructions by suppressing background noise and image artefacts, achieving ~ 1.9 times higher signal-to-noise ratios and an increase of the intersection over union (IoU) from 16.4% to 61.9%. Thus, the proposed framework could be helpful for reducing complications during percutaneous needle insertions by accurate identification of clinical needles in photoacoustic imaging.

Index Terms—Photoacoustic imaging, needle visibility, light emitting diode, deep learning, minimally invasive procedures.

I. INTRODUCTION

US imaging is widely used for guiding minimally invasive percutaneous procedures such as peripheral nerve blocks [1], tumour biopsy [2] and fetal blood sampling [3]. During these procedures, a metallic needle is inserted percutaneously into the body towards the procedure target under real-time US guidance. Accurate and efficient identification of the procedure target and the needle is of paramount importance to ensure

This work was supported by the Wellcome Trust [203148/Z/16/Z, WT101957, 203145Z/16/Z], the Engineering and Physical Sciences Research Council (EPSRC) (NS/A000027/1, NS/A000050/1, NS/A000049/1), and King's-China Scholarship Council PhD Scholarship Program (K-CSC).

Mengjie Shi, Tianrui Zhao, Tom Vercauteren, and Wenfeng Xia are with the School of Biomedical Engineering & Imaging Sciences, King's College London, SE1 7EH London, U.K.

Simeon J. West is with the Department of Anaesthesia, University College Hospital, NW1 2BU London, U.K.

Adrien E. Desjardins is with the Wellcome/EPSRC Centre for Interventional and Surgical Sciences, University College London, London W1W 7TY, U.K., and with the Department of Medical Physics and Biomedical Engineering, University College London, WC1E 6BT London, U.K.

Correspondence should be addressed to: Wenfeng Xia (wenfeng.xia@kcl.ac.uk)

the efficacy and safety of the procedures. Despite a number of prominent advantages associated with US imaging such as its real-time imaging capability, high affordability and accessibility, it suffers from intrinsically low soft tissue contrast that sometimes results in insufficient visibility of critical tissue structures such as nerves and small blood vessels. Moreover, visibility of clinical needles with US imaging is strongly dependent on the insertion angle and depth of the needle. With steep insertion angles, US reflections can be readily outside of the transducer aperture, leading to poor ultrasound visibility. Loss of visibility of tissue targets or the needle can cause significant complications [4].

Photoacoustic (PA) imaging has been of growing interest in the past two decades for its various potential preclinical and clinical applications owing to its unique ability to resolve spectroscopic signatures of tissues at high spatial resolution and depths [5]–[7]. In recent years, several research groups have proposed the combination of US and PA imaging for guiding minimally invasive procedures by offering complementary information to each other, with US imaging providing tissue structural information and PA imaging identifying critical tissue structures and invasive surgical devices such as metallic needles [8]–[11]. Recently, laser diodes (LDs) and light emitting diodes (LEDs) have shown promise as an alternative to commonly used solid-state lasers as PA excitation sources because of their compact sizes and low costs, which could be beneficial for clinical translation [12]. However, compared to solid-state lasers, LDs and LEDs usually have a much lower pulse energy, resulting in sub-optimal image quality and a lower signal-to-noise ratio (SNR).

Deep learning (DL) has been proved as a powerful tool for signal and image processing tasks in medical imaging [13]–[15]. Recently it has been applied in PA imaging especially photoacoustic tomography (PAT) [16] where DL approaches could be used to process raw channel data or post-beamformed data to improve image quality [17]–[20] as well as for image segmentation or classification tasks based on reconstructed PA images [21], [22].

Lately, DL has been used by several research groups for improving the imaging quality of LED-based PA/US imaging systems. Anas *et al.* [23] exploited the use of a combination of a convolutional neural network (CNN) and a recurrent neural network (RNN) to enhance the quality of PA images by leveraging both the spatial features and temporal information in repeated PA image acquisitions. Convincing improvement has been achieved in imaging point targets over the conven-

tional averaging approach as well as the CNN-only method. Kuniyil Ajith Singh *et al.* [12] proposed to use a U-Net model to improve the SNR by training a neural network using PA images acquired by an improved PA imaging system with a higher laser energy and broadband ultrasound transducers. The pre-trained model was proven effective with LED-based PA images acquired from phantoms. Hariri *et al.* [24] proposed a multi-level wavelet-CNN to enhance noisy PA images associated with low fluence LED illumination by learning from PA images acquired with high fluence illumination sources. Enhancements were achieved on unseen *in vivo* data with improved image contrast. Most recently, Kalloor Joseph *et al.* [25] developed a generative adversarial network (GAN)-based framework for PA image reconstruction to mitigate the impact of the limited aperture and bandwidth of the ultrasound transducer. The proposed model was trained on simulated images from artificial blood vessels and validated on *in vivo* measurements of the human forearm. They reported a considerable enhancement of the GAN predicted PA images, showing great promise of employing GANs for PA image enhancement.

Whilst prominent attention has been attracted on improving the visualisation of tissue structures, interestingly not much effort has been made to improve the needle visibility in PA imaging. In this work, we proposed a DL-based framework to enhance the visibility of clinical needles with PA imaging for guiding minimally invasive procedures. As clinical needles have relatively simple geometries compared to biological tissues such as blood vessels, a hybrid method was used for generating semi-synthetic training dataset. Validation of the trained neural network was performed with tissue-mimicking phantoms, *ex vivo* tissue and human fingers *in vivo* in comparison with a baseline method called Standard Hough Transform. To the best of our knowledge, this is the first work that exploits DL for improving needle visualisation with PA imaging and also the first work that utilizes semi-synthetic training datasets for DL in PA imaging.

II. MATERIALS AND METHODS

A. Semi-synthetic Dataset Generation

The process of semi-synthetic dataset generation comprised three main steps as shown in Fig. 1: 1) the generation of synthetic sensor data from needles; 2) acquisition of *in vivo* data to account for background photoacoustic signals originated from biological tissue; 3) image reconstruction with raw channel data combining synthetic and measurement data.

Simulations of the sensor data originated from the needle were performed using the k-Wave toolbox [26]. Initial pressure distribution maps were created by simulating the optical fluence distributions on the needle shaft using Monte Carlo simulations [27]. A $4.0\text{ cm} \times 4.0\text{ cm}$ area with a grid size of 0.1 mm containing a homogeneous optical property distribution was constructed to represent the background tissue, with a refractive index, a optical scattering coefficient and an anisotropy of 1.4 , 100 cm^{-1} and 0.9 , respectively [28]. Three absorption coefficients of 0.1 , 0.15 , 0.2 were used. A homogeneous photo beam with a finite size of 38.4 mm was

applied to the surface of the simulation area. Each simulation was run for around 10 minutes with approximate $100\,000$ photon packets.

A linear array of 128 ultrasound transducer elements (with a pitch of 0.3 mm over a total length of 38.4 mm) was used to receive the generated photoacoustic signals from the initial pressure distributions maps assigned to a forward model in k-Wave that simulates the photoacoustic signal generation and propagation. The ultrasound transducer was assigned a central frequency of 9 MHz and a fractional -6 dB bandwidth of 80.9% based on the specifications of a LED-based PA/US imaging system (see Sec.II-C). The radio-frequency (RF) data collected by the transducer elements were successively down sampled to 40 MHz to match the sampling rate of the measured data.

In vivo data for background vasculature were collected by imaging the fingers of 13 healthy human volunteers using the LED-based PA/US imaging system (AcousticX, CYBER-DYNE INC, Tsukuba, Japan). Details of the imaging system is provided in Sec.II-C. At last, for each semi-synthetic image, a pair of 2D data matrices (1024×128) consisted of RF data from a simulation on a needle and a measurement on a human finger were added to form a single 2D data matrix and then fed to a Fourier domain algorithm for image reconstruction [29].

Simulations were conducted for needles with different insertion depths and angles, spanning from 5 mm to 25 mm with an increment of 5 mm , and from 20 degrees to 65 degrees with a step of 5 degrees, respectively. Following the workflow, a total number of 2000 semi-synthetic images with substantial variations on both the needle targets and background were prepared. The datasets for training and testing was given by 2000 image pairs that formed by these semi-synthetic images and their corresponding needle images with initial pressure distributions. These images had the same dimension as the acquired PA and US images of $40.32\text{ mm (X)} \times 39.42\text{ mm (Z)}$ according to the geometry of the linear transducer and a time step of 1024 at a 40 MHz sampling rate. Both original PA and semi-synthetic images were interpolated to 578×565 pixels with an uniform pixel size of $70\text{ }\mu\text{m} \times 70\text{ }\mu\text{m}$. To facilitate network implementations, the images were cropped to 512×512 pixels by removing the corresponding rows from top to bottom and the same number of columns from left to centre and right to centre respectively.

B. Network Implementation

The deep neural network used for this work was modified from the U-Net [16]. As shown in Fig. 2, this network had 3 scales in total. Following an encoder path, each scale consisted of two convolutional layers followed by a 2×2 max pooling layer. For the decoder path, similarly, each scale contained two convolutional layers but followed by a transposed convolutional layer with an up-sampling factor of 2. The dataset was split into train, test and validation sets with a ratio of 8:1:1. Our network was firstly trained with the input pairs with a smaller resolution of 128×128 pixels resized from the original size of 512×512 pixels via bicubic

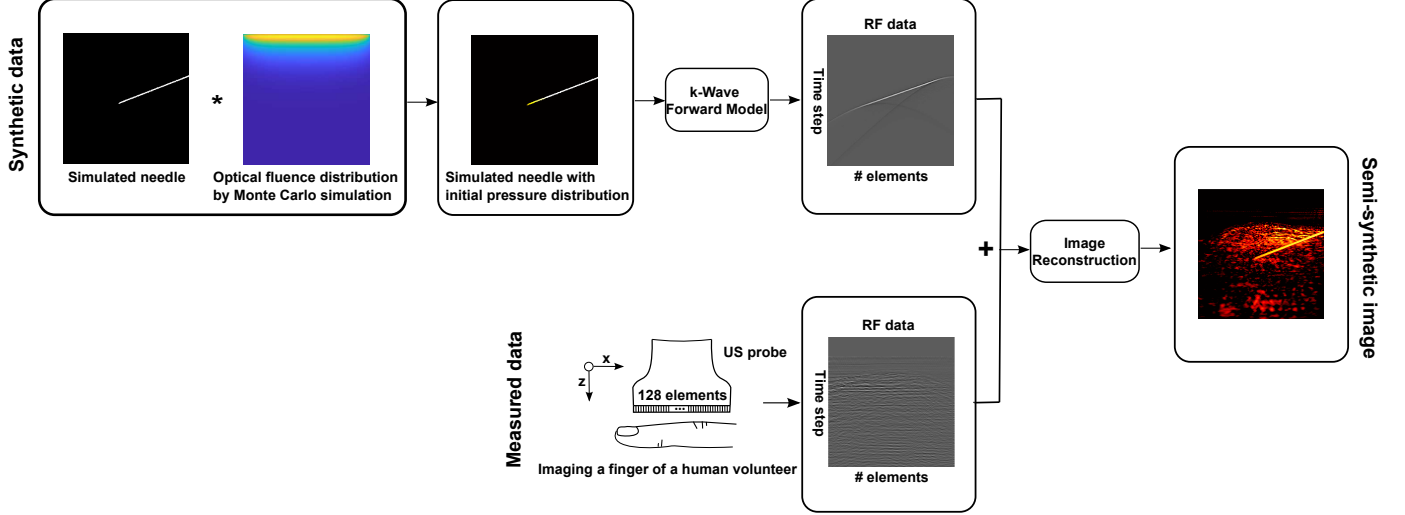


Fig. 1. The proposed hybrid method for semi-synthetic dataset generation. Top row: synthetic radio-frequency (RF) sensor data generation from simulated needle. Bottom row: acquisition of sensor data from human finger vasculature *in vivo* as background. Note: A Fourier domain algorithm was used for image reconstruction on raw data obtained by combining synthetic and measured data. Semi-synthetic image was displayed on a decibel scale ranging from -45 to 0 dB.

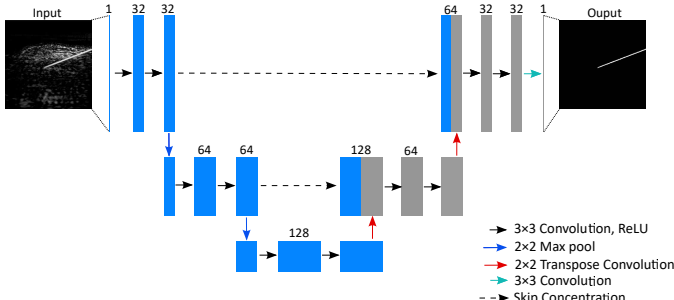


Fig. 2. Network architecture based on a modified U-Net. Semi-synthetic images were converted to greyscale as inputs. A ground truth was the corresponding needle image with initial pressure distribution. The U-Net was trained to enhance the visibility of needle in PA images.

interpolation, and then applied on unseen real data also with a resized dimension of 256×256 pixels for further validation.

Our network was implemented in Python using PyTorch v1.2.0. Training was performed for 5000 iterations with a batch size of 4 that minimised the mean square error (MSE) loss using ADAM optimiser (Initial learning rate: 0.001) and on the Google CoLaboratory platform using a Tesla P100-PCIE-16GB GPU.

C. Acquisition of Phantom, Ex vivo and In vivo Data for Validation

Evaluation of the trained neural network was implemented on acquired PA images using AcousticX with needle (20G, BD, USA) insertions into a blood-vessel-mimicking phantom, pork joint tissue *ex vivo* and human fingers *in vivo* (needle outside of tissue; see Supplementary Materials; Video S1). Experiments on human volunteers were approved by the King's College London Research Ethics Committee (study reference: HR-18/19-8881).

The blood-vessel-mimicking phantom was created by arranging several carbon fibre bundles in a plastic box filled

with 1% Intralipid dilution (Intralipid 20% emulsion, Scientific Laboratory Supplies, UK) that had an estimated optical reduced scattering coefficient of 0.96 mm^{-1} at 850 nm [30].

Detailed description of the LED-based PA/US imaging system, AcousticX, can be found elsewhere [31]. Here, briefly, PA excitation light is delivered from two LED arrays that sandwiches the linear array US probe at a fixed angle. Each array consists of four rows of LEDs with 36 elements of $1 \text{ mm} \times 1 \text{ mm}$ on each row. The LED arrays can be driven at different pulse repetition frequencies from 1 kHz to 4 kHz, and the maximum optical energy of each pulse from each array is $200 \mu\text{J}$. The LED pulse duration is controllable between 30 ns to 150 ns. In this study, a pulse width of 70 ns at 850 nm was selected for optimal energy efficiency. The illumination area formed by the LED arrays was approximately a rectangle ($50 \text{ mm} \times 7 \text{ mm}$), resulting in an optical fluence of 0.11 mJ/cm^{-2} at the maximum pulse energy of $400 \mu\text{J}$.

RF data for PA and US imaging were collected simultaneously from 128 channels on the probe with sampling rates of 40 MHz and 20 MHz, respectively. Interleaved PA and US imaging can be performed in real-time with image reconstruction performed on a graphics processing unit (GPU). Meanwhile, a maximum of 1536 PA frames and 1536 US frames corresponding to a total duration of 20s could be saved in memory at one time available for offline reconstruction.

The RF data of one PA or US frame was a 2D matrix with a dimension of 1024×128 . The first 150 (out of 1024) timesteps were zeroed before image reconstruction to remove strong LED-induced noise that spanned across the upper 5 mm depth in PA and US images. In our study, averaging over 128 frames was implemented on both PA and US images for pre-denoising before network validation.

D. Post-processing and Evaluation Protocol

A post-processing algorithm based on maximum contour selection was developed for further improving the outcomes

of the trained neural network [32]. It detected all contours in the outputs of the trained model and selected the maximum contour as the one from the needle by counting the number of pixels on each contour boundary.

To obtain the ground truth for performance evaluation, manual labelling was used based on the prior knowledge of the needle dimensions [33]. The needle was annotated as a rectangular area where the length was determined by the centreline of the needle while the width was equal to its real dimension (nominal outer diameter is 0.902 mm for 20G needles). The needle tips had a good contrast on US images when it was surrounded by water in the liquid-based tissue-mimicking phantoms but had poor visibility for *ex vivo* and *in vivo* measurements. Therefore, solid glass spheres (0-63 µm, Boud Minerals Limited, UK) were injected after being diluted with water to enhance the contrast of the tips, thus improving the accuracy and precision of manual labelling.

In this study, SNR and several evaluation metrics that are often used in the context of medical image segmentation were employed for performance evaluation including True Positive Rate (TPR), Positive Predictive Value (PPV), Intersection over Union (IoU), and Average Surface Distance (ASD) shown in (1)-(3).

$$TPR = \frac{TP}{TP + FN} \quad (1)$$

$$PPV = \frac{TP}{TP + FP} \quad (2)$$

$$IoU = \frac{TP}{TP + FP + FN} \quad (3)$$

where TP , FP , FN represent true positives, false positives, and false negatives for the needle, respectively, and ASD was defined as:

$$ASD = \frac{1}{|S(A)| + |S(B)|} \left(\sum_{a \in S(A)} \min_{b \in S(B)} \|a - b\| + \sum_{b \in S(B)} \min_{a \in S(A)} \|b - a\| \right) \quad (4)$$

in which $S(A)$ and $S(B)$ denote the set of surface pixels of A , B which were the outcomes of the contour detection algorithm.

SNR was defined as $SNR = S / \sigma$, where S is the mean signal amplitude and σ is the standard deviation of noise. The signal region was chosen as the region of needle from the ground truth.

Thresholding especially on conventional reconstruction was performed before calculating these metrics. Receiver Operating Characteristic (ROC) curves were drawn for each validation to determine optimised thresholds and can be found in Supplementary Materials.

E. Comparison with Baseline Method

Further evaluation on the performance of the trained neural network was conducted by comparing it to a classical baseline method for line detection, namely standard Hough transform (SHT) [34]. The SHT is initially designed to identify straight

lines in images. The SHT employs the parametric representation of a straight line which is also called Hesse normal form and can be expressed as:

$$r = x\sin\theta + y\cos\theta \quad (5)$$

where r is the shortest distance from the origin to the line. θ measures the angle between the x-axis and the perpendicular projection from the origin point to the line. Therefore, a straight line can be associated with a pair of parameters (r, θ) , corresponding to a sinusoidal curve in Hough space. A few points on the same straight line will produce a set of sinusoidal curves that cross the same point (r, θ) which exactly represents that line. In this study, the SHT was implemented by a two-dimensional matrix whose columns and rows were used to save the r and θ values respectively. For each point in the image, r was calculated for each θ , leading increments of that bin in the matrix. Finally, the potential straight lines in the image were extracted by selecting the local maxima from the accumulator matrix.

III. RESULTS

A. Blood-vessel-mimicking Phantoms

The results of imaging on blood-vessel-mimicking phantoms are shown in Fig. 3. Compared to conventional reconstruction, improvements by the U-Net are quite noticeable in terms of removing background noise and artefacts around the needle. The trained neural network precisely identified and enhanced the needle without being substantially affected by the artificial vessels in the background that share similar line-shape features with the needle. The false positives in the U-Net enhanced images could be efficiently removed without undermining the needle extraction by post-processing with maximum contour selection. Quite noticeably, the trained model kept performing well on the image with a low SNR and strong artefacts in Fig. 3 (d). The overlays show that the needle from the U-Net enhancement corresponded well to that on original conventional reconstruction and provided precious indications about the needle locations on US images where the needle was barely visible.

Evaluation metrics were calculated and reported in Table I. The SNR values by the U-Net enhancement were significantly higher than those by conventional reconstruction. Other metrics especially PPV, representing the proportion of true positives out of all positive predictions, showed a great improvement on the U-Net enhancement over conventional reconstruction from 3.1% to 47.8%. The U-Net enhancement showed a decrease on TPR of 46.9% compared to 89.7% by conventional reconstruction. Thresholding on conventional reconstruction affected the measurement of TPR by misclassifying a certain number of background noise as signals from the needle. Therefore, TPR is not convincingly reliable for performance comparison in this case but indicates the differences of their performances in some degree. Additionally, ASD was calculated and compared across different methods. For conventional reconstruction, ASD was exceptionally large due to the background signals, but this metric substantially decreased with the proposed network.

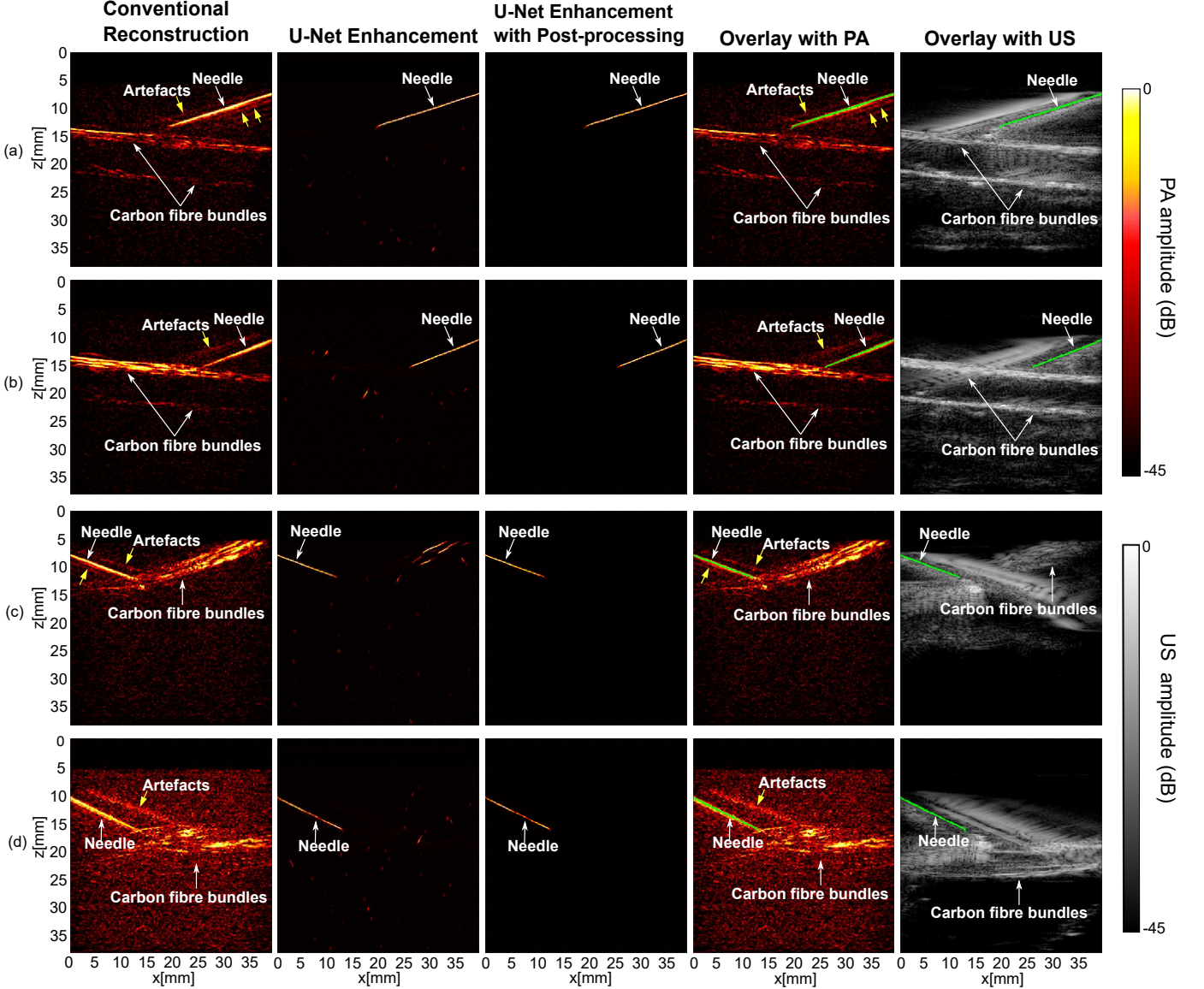


Fig. 3. Photoacoustic imaging with needle insertions into a blood-vessel-mimicking phantom with conventional reconstruction, U-Net enhancement and U-Net enhancement with post-processing.

TABLE I
QUANTITATIVE EVALUATION OF THE TRAINED NEURAL NETWORK USING A BLOOD-VESSEL-MIMICKING PHANTOM

Metrics	CR ^a	U-Net Enhancement	U-Net Enhancement with Post-processing	Self-generated Needle
SNR	6.289	26.877	-	-
IoU	8.5%	31.1%	38.9%	62.1%
PPV	8.6%	47.8%	98.6%	83.9%
TPR	89.7%	46.9%	39.9%	70.1%
ASD	9.060E+05	5015.793	12.276	3.850

^aConventional Reconstruction

B. Pork Joint Tissue Ex vivo

Fig. 4 and Table II shows the qualitative and quantitative performances of the trained model using images from pork joint *ex vivo* tissue. In this experiment, an inherent gap

between the imaging probe and the skin surface of the joint forced a larger insertion depth compared to the liquid-based blood-vessel-mimicking phantom, resulting in considerable degradation in PA images, which however did not impede the enhancements by the trained U-Net. The U-Net model maintained a good performance of subduing the background noise and improving the needle visualisation. In Fig. 4 (b) and (d), the enhancement of the needle suffered from certain decline at the distal region of the needle where the SNRs were sub-optimal due to the deep insertion. In Table II, the U-Net enhancement had a higher SNR value compared to the conventional reconstruction (11.755 and 37.172 respectively). The U-Net enhancement also achieved the PPV of 54.4% which was 2.8% higher than that of the conventional reconstruction.

The relationship between the number of averaged frames (or imaging speed) and the SNRs of the needle images with

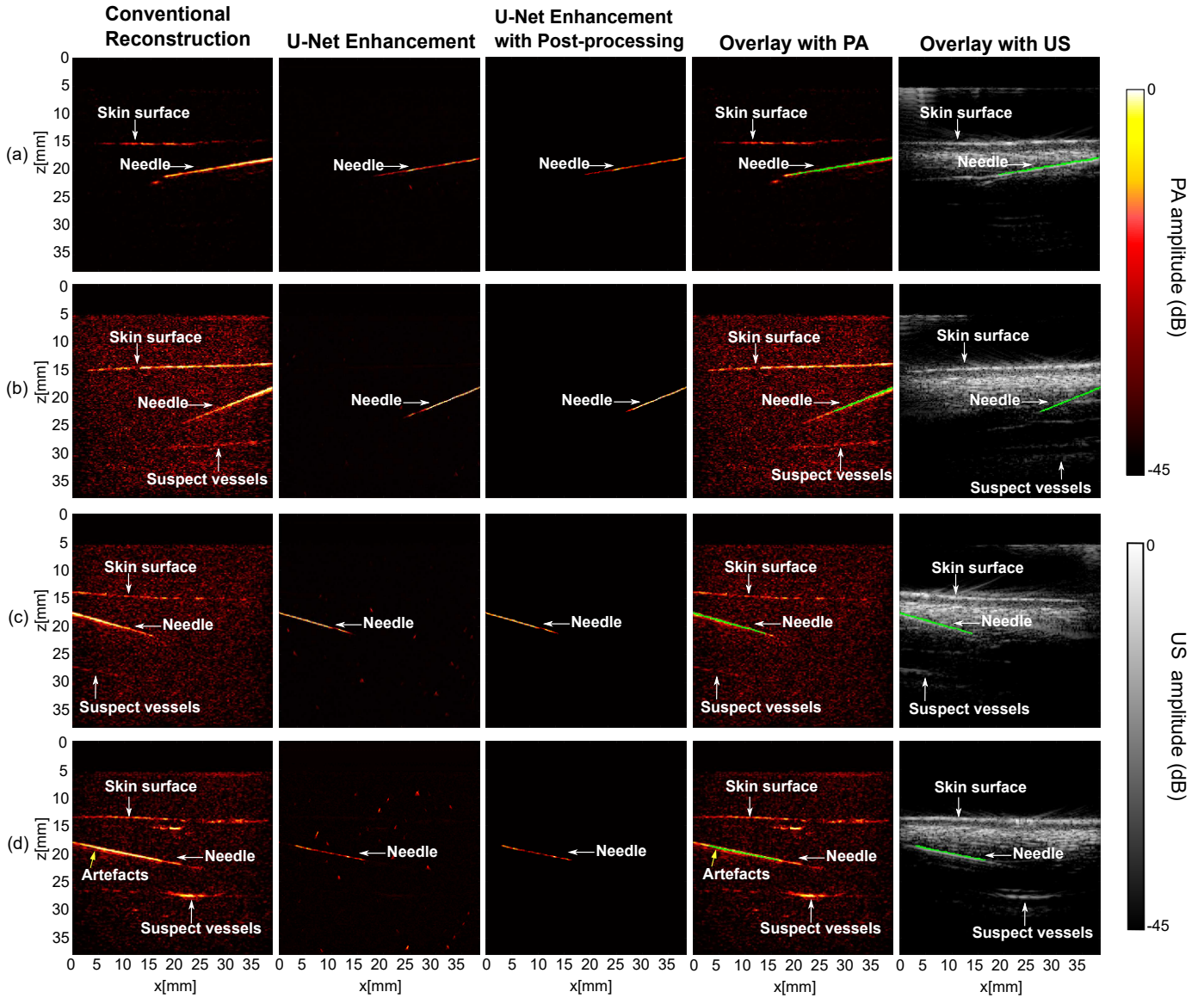


Fig. 4. Photoacoustic imaging with needle insertions into *ex vivo* tissue with conventional reconstruction, U-Net enhancement, and U-Net enhancement with post-processing.

TABLE II
QUANTITATIVE EVALUATION OF THE TRAINED NEURAL NETWORK USING EX VIVO NEEDLE IMAGES

Metrics	CR ^a	U-Net Enhancement	U-Net Enhancement with Post-processing	Self-generated Needle
SNR	11.755	37.172	-	-
IoU	13.4%	36.6%	33.2%	55.8%
PPV	14.1%	54.4%	98.6%	84.7%
TPR	86.0%	45.1%	33.4%	62.8%
ASD	7.438E+05	2628.722	60.337	14.963

^aConventional Reconstruction

the U-Net enhancement and conventional reconstruction was investigated and compared as shown in Fig. 5. The number of averaged frames was gradually increased from 1 to 24 which was equivalent to different imaging speeds (frames per second)

if the data collection time was considered. Four groups of *ex vivo* needle images (20 images for each group) with varying insertion depths and angles were used in this investigation. Fig. 5 shows that the trained U-Net outperformed the conventional reconstruction over all averages. For example, in Fig. 5 (a)-(i), the needle can be regarded absent due to massive background noise. In this case, the trained model improved the images by significantly reducing the noise whereas the conventional reconstruction could hardly automate that using empirical thresholds.

C. *In vivo* Imaging

Fig. 6 shows the results of PA imaging with needle insertion outside of a finger of a human volunteer. A main digital artery which has a similar two-layered feature is apparent on PA images. A 22s video was recorded during the needle insertion (see Supplementary Materials; Video S2). Fig. 6

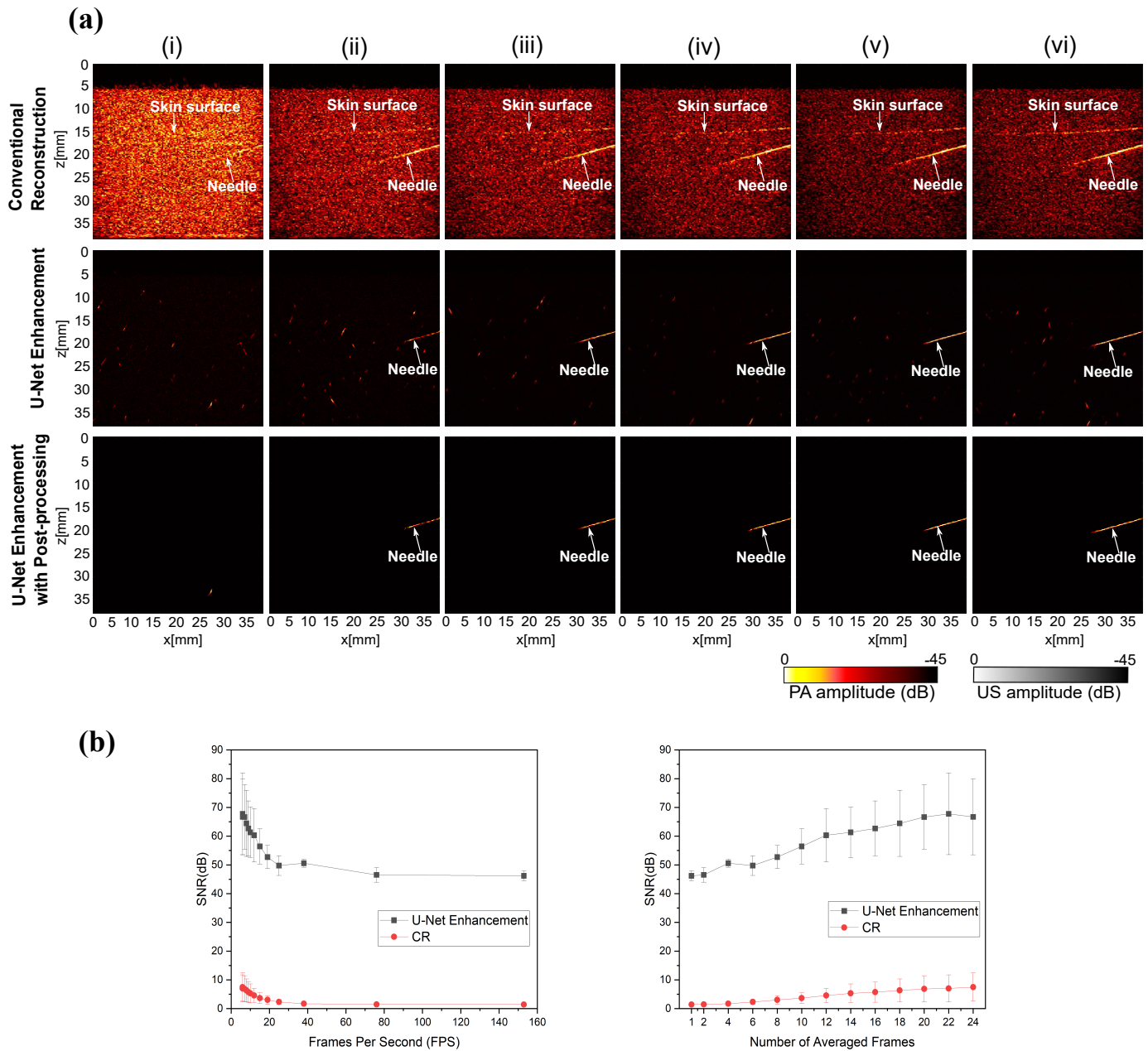


Fig. 5. (a) Photoacoustic images of needle insertions into pork joint *ex vivo* tissue with conventional reconstruction, U-Net enhancement and U-Net enhancement with post-processing under different number of averaged frames: from (i) to (vi) are 4, 8, 12, 16, 20, 24 respectively; (b) SNRs of *ex vivo* needle images with conventional reconstruction (CR) and U-Net enhancement under different frames per second (FPS) (left) and different number of averaged frames (right). Data represent average values and error bars represent standard deviations.

demonstrates four image frames acquired at different time points with the conventional reconstruction and the overlay images with PA and US after the U-Net enhancement and SHT. Processing these frames using SHT resulted in good extractions of the needle but high false positive rates. This is because the performance of SHT is highly sensitive to the choice of the hyperparameters and it is thus non-trivial to do fine-tuning for each frame based on the observations of the needle when processing the whole video sequence. In comparison, the trained neural network manifested a good ability of generalization and robustness. The needle with different insertion lengths, depths and angles was well extracted and

enhanced during this dynamic process, improving the overall image quality.

In particular, as shown in Table III, the SNR was 18.291 when conventional reconstruction was applied, which was substantially increased to 52.541 with the U-Net enhancement. In terms of evaluation metrics, the U-Net enhancement resulted in a significant increase of PPV from 17.0% to 66.1%. The PPV value was further increased to 94.6% after the post-processing. For the self-generated needle, this value decreased to 76.3% due to the estimation errors happened at the edges of the needle areas. Improvements by the trained neural network can also be quantified using ASD. For conventional reconstruction, ASD

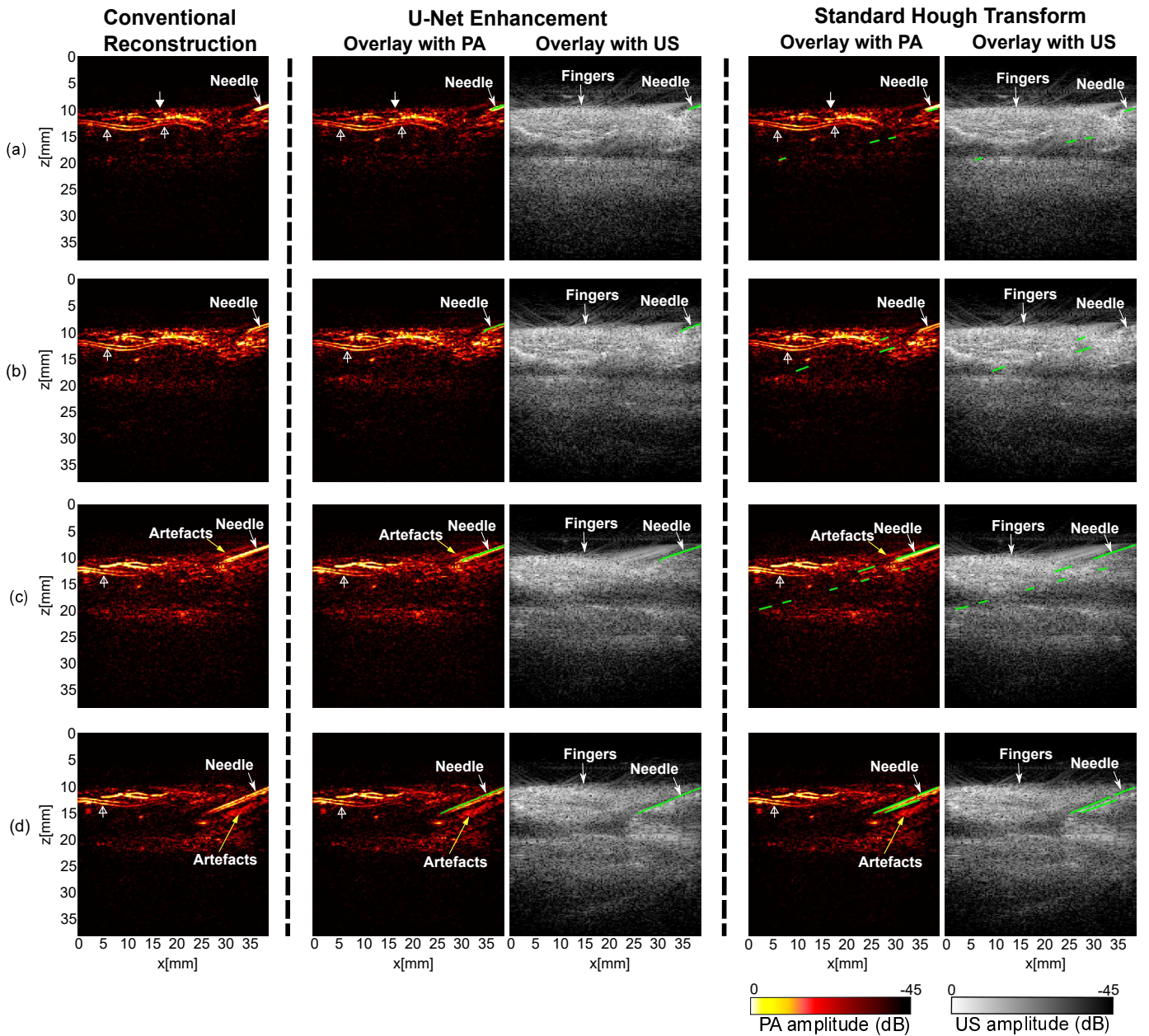


Fig. 6. Photoacoustic imaging with needle insertions into human fingers *in vivo* with conventional reconstruction, U-Net enhancement, and Standard Hough Transform. Signals from the skin surface are indicated by triangle wide arrows, and signals that may be from digital arteries are indicated by hollow triangle wide arrows. The outcomes of U-Net enhancement and Standard Hough Transform are denoted by green lines in PA and US overlay. (a) - (d) are from reconstructed photoacoustic image sequence recorded during needle insertions in real time.

was still very large even with an optimised threshold, indicating a large number of false positives occurred in the images. In contrast, a significant decrease in ASD happened with the U-Net enhancement. Further improvements can be obtained after removing the most majority of false positives by post-processing the images after U-Net enhancement. For the self-generated needles, ASD was as small as 2.105, implying the high accuracy of the needle identification using the proposed neural network.

D. Impact of Needle Diameters

To verify the U-Net's generalization on enhancing PA visibility of clinical metallic needles in different sizes, needles

with 5 different diameters (16G, 18G, 20G, BD, USA; 25G, 30G, Meso-relle, Italy) were imaged using AcousticX when being inserted into pork joint *ex vivo* tissue. Photographs and some representative validation results for each diameter are included in Supplementary Materials. The diameters of the needles had no significant impact on the performance of the trained U-Net. Even for the 30G needle, although the corresponding images suffered from a low SNR due to the small diameter, the trained U-Net was able to accurately extract the needle targets with a great continuity. The enhancements by the U-Net were quantified using SNR and other segmentation metrics (see Supplementary Materials; Table I). The proposed U-Net model had a better quantitative performance over con-

TABLE III
QUANTITATIVE EVALUATION OF THE TRAINED NEURAL NETWORK USING *IN VIVO* NEEDLE IMAGES

Metrics	CR ^a	U-Net Enhancement	U-Net Enhancement with Post-processing	Self-generated Needle
SNR	18.291	52.541	-	-
IoU	16.4%	39.0%	41.7%	61.9%
PPV	17.0%	66.1%	94.6%	76.3%
TPR	91.5%	49.6%	42.6%	74.0%
ASD	7.127E+05	2426.017	17.217	2.105

^aConventional Reconstruction

ventional reconstruction in terms of all the metrics, except for TPR where the diameter of the enhanced needle also mattered. The proposed network also efficiently removed background noise and artefacts in PA images, resulting in an averaged SNR around 6.6 times higher in comparison with conventional reconstruction. The needles with different sizes identified by the U-Net corresponded well to the conventional PA reconstructions, as indicated by the substantial improvements on averaged IoU and ASD (7.1% vs. 33.53% and 3.2489E+05 vs. 1193.7220 respectively).

IV. DISCUSSION & CONCLUSIONS

Previous works on deep learning in PA imaging mainly focused on image reconstruction and post-processing such as denoising and artefacts removal. In this work, we are the first to apply DL to improve needle visualisation with PA imaging for minimally invasive guidance. Further, differing from previous works, we used a hybrid method for the generation of the training dataset combining simulated and measured data. According to our experimental results (not shown), the simulated optical fluence distribution had a minimal effect on the performance of the proposed model when validated on unseen real needle images even with deep insertion angles. This is because the DL-based method was able to enhance the visualisation of the needle by learning its relatively simple spatial features that remained largely consistent.

During minimally invasive procedures, accurate and clear visualisation of the needle is essential for successful outcomes. PA imaging can greatly improve the visualisation of the needle as compared to US imaging but the image quality in terms of SNR with the LED light source is still sub-optimum due to the low pulse energy. Frame averaging is effective for reducing background noise but at the cost of the imaging speed and introduces movement artefacts. Further, blood vessels in the background with similar line-shape structures to the needle are sometimes regarded as visual disturbances for clinicians to accurately track the needle. Finally, line artefacts above or beneath the needle shaft are often non-negligible that can lead to misinterpretation of the needle position. Based on the validation results, our proposed model achieved substantial enhancement on the needle visualisation by greatly suppressing the random noise and artefacts, as well as efficiently extract the needle with high accuracy and precision. The post-processing algorithm based on contour selection further optimised the enhancements by getting rid of the random false positives.

Quantitative performance analysis with IoU, PPV and ASD indicated that the proposed DL-based model with semi-synthetic dataset performed well on enhancing needle visibility using unseen phantom, *ex vivo* and *in vivo* data with high accuracy and precision. It is noted that the proposed model failed to achieve high TPRs as compared to the conventional reconstruction. This is because with the conventional reconstruction, massive noise and artefacts were also extracted and classified as the true positives from the background and the false negatives were relatively tiny, followed by high TPRs. In contrast, the needle was predicted as a straight line in the outputs by the U-Net compared to the inputs. This could be explained by the feature extraction behaviour of the trained network, but it is not beneficial when evaluating metrics that count the needle as a region of interest such as TPR. Therefore, manual labelling of the needle was investigated and used for metrics evaluation, showing that the learnt outcomes by the proposed network remained accurate and precise considering the quantitative improvements over all metrics.

We also compared the DL-based method with a conventional line detection algorithm SHT with *in vivo* measurements. SHT performed quite well in some cases with carefully chosen critical parameters, but it was easily affected by imperfection errors from the former edge detection step. Further it also highly relied on handcrafting some decision criteria such as empirical values of r and θ that are directly related to the detection efficiency, and it is impractical during dynamic procedures where the effective length of the needle varies in each frame.

The proposed DL-based framework significantly enhanced the needle visualisation with PA imaging and thus could be useful for guiding minimally invasive procedures that involve percutaneous needle insertions. The performance of the proposed framework was validated by PA images acquired with needle insertions into blood-vessels-mimicking phantoms, *ex vivo* tissue and *in vivo* measurements with human fingers. However, the enhancement was also sensitive to the SNRs of the images. More importantly, the visibility of the needle tip was still limited to a depth of around 1 cm with *in vivo* measurements. In the future, deep neural networks could be applied for real-time denoising [24] as an alternative to frame-to-frame averaging to improve the imaging depth. For needle tip visualisation, a fibre-optic US transmitter could be integrated within the needle cannula so that the needle tip can be unambiguously visualised in PA imaging with high SNRs [35]. Light-absorbing coatings based on elastomeric nanocomposites could also be applied to the needle shaft for enhancing its visualisation for guiding minimally invasive procedures [36].

REFERENCES

- [1] K. J. Chin, A. Perlas, V. W. S. Chan, and R. Brull, "Needle Visualization in Ultrasound-Guided Regional Anesthesia: Challenges and Solutions," *Reg Anesth Pain Med*, vol. 33, no. 6, pp. 532–544, 2008.
- [2] T. H. Helbich, W. Matzek, and M. H. Fuchsäger, "Stereotactic and ultrasound-guided breast biopsy," *Eur Radiol*, vol. 14, no. 3, pp. 383–393, 2004.

[3] F. Daffos, M. Capella-Pavlovsky, and F. Forestier, "Fetal blood sampling during pregnancy with use of a needle guided by ultrasound: A study of 606 consecutive cases," *Am J Obstet Gynecol*, vol. 153, no. 6, pp. 655–660, 1985.

[4] J. P. Rathmell, H. T. Benzon, P. Dreyfuss, M. Huntoon, M. Wallace, R. Baker, K. D. Riew, R. W. Rosenquist, C. Aprill, N. S. Rost, A. Buvanendran, D. S. Kreiner, N. Bogduk, D. R. Fournier, E. Fraifeld, S. Horn, J. Stone, K. Vorenkamp, G. Lawler, J. Summers, D. Kloft, D. O'Brien, and S. Tutton, "Safeguards to prevent neurologic complications after epidural steroid injections: Consensus opinions from a multidisciplinary working group and national organizations," *Anesthesiology*, vol. 122, no. 5, pp. 974–984, 2015.

[5] L. V. Wang and J. Yao, "A practical guide to photoacoustic tomography in the life sciences," *Nat Methods*, vol. 13, no. 8, pp. 627–638, 2016.

[6] V. Ntziachristos, "Going deeper than microscopy: The optical imaging frontier in biology," *Nat Methods*, vol. 7, no. 8, pp. 603–614, 2010.

[7] P. Beard, "Biomedical photoacoustic imaging," *Interface Focus*, vol. 1, no. 4, pp. 602–631, 2011.

[8] M. Kuniyil Ajith Singh, W. Steenbergen, and S. Manohar, "Handheld Probe-Based Dual Mode Ultrasound/Photoacoustics for Biomedical Imaging," in *Frontiers in Biophotonics for Translational Medicine: In the Celebration of Year of Light (2015)*, ser. Progress in Optical Science and Photonics, M. Olivo and U. S. Dinish, Eds. Singapore: Springer, 2016, pp. 209–247.

[9] S. Park, J. Jang, J. Kim, Y. S. Kim, and C. Kim, "Real-time Triple-modal Photoacoustic, Ultrasound, and Magnetic Resonance Fusion Imaging of Humans," *IEEE Transactions on Medical Imaging*, vol. 36, no. 9, pp. 1912–1921, 2017.

[10] W. Xia, D. I. Nikitichev, J. M. Mari, S. J. West, R. Pratt, A. L. David, S. Ourselin, P. C. Beard, and A. E. Desjardins, "Performance characteristics of an interventional multispectral photoacoustic imaging system for guiding minimally invasive procedures," *JBO*, vol. 20, no. 8, p. 086005, 2015.

[11] T. Zhao, A. E. Desjardins, S. Ourselin, T. Vercauteren, and W. Xia, "Minimally invasive photoacoustic imaging: Current status and future perspectives," *Photoacoustics*, vol. 16, p. 100146, 2019.

[12] M. Kuniyil Ajith Singh and W. Xia, "Portable and Affordable Light Source-Based Photoacoustic Tomography," *Sensors*, vol. 20, no. 21, p. 6173, 2020.

[13] A. S. Lundervold and A. Lundervold, "An overview of deep learning in medical imaging focusing on MRI," *Zeitschrift für Medizinische Physik*, vol. 29, no. 2, pp. 102–127, 2019.

[14] S. Liu, Y. Wang, X. Yang, B. Lei, L. Liu, S. X. Li, D. Ni, and T. Wang, "Deep Learning in Medical Ultrasound Analysis: A Review," *Engineering*, vol. 5, no. 2, pp. 261–275, 2019.

[15] I. Domingues, G. Pereira, P. Martins, H. Duarte, J. Santos, and P. H. Abreu, "Using deep learning techniques in medical imaging: A systematic review of applications on CT and PET," *Artif Intell Rev*, vol. 53, no. 6, pp. 4093–4160, 2020.

[16] A. Hauptmann and B. Cox, "Deep learning in photoacoustic tomography: Current approaches and future directions," *J. Biomed. Opt.*, vol. 25, no. 11, 2020.

[17] S. Antholzer, M. Haltmeier, R. Nuster, and J. Schwab, "Photoacoustic image reconstruction via deep learning," in *Photons Plus Ultrasound: Imaging and Sensing 2018*, vol. 10494. SPIE, 2018, pp. 433–442.

[18] N. Davoudi, X. L. Deán-Ben, and D. Razansky, "Deep learning optoacoustic tomography with sparse data," *Nat Mach Intell*, vol. 1, no. 10, pp. 453–460, 2019.

[19] D. Allman, A. Reiter, and M. A. L. Bell, "Photoacoustic Source Detection and Reflection Artifact Removal Enabled by Deep Learning," *IEEE Transactions on Medical Imaging*, vol. 37, no. 6, pp. 1464–1477, 2018.

[20] N. Awasthi, G. Jain, S. K. Kalva, M. Pramanik, and P. K. Yalavarthy, "Deep Neural Network-Based Sinogram Super-Resolution and Bandwidth Enhancement for Limited-Data Photoacoustic Tomography," *IEEE Transactions on Ultrasonics, Ferroelectrics, and Frequency Control*, vol. 67, no. 12, pp. 2660–2673, 2020.

[21] Y. E. Boink, S. Manohar, and C. Brune, "A Partially-Learned Algorithm for Joint Photo-acoustic Reconstruction and Segmentation," *IEEE Transactions on Medical Imaging*, vol. 39, no. 1, pp. 129–139, 2020.

[22] D. Allman, F. Assis, J. Chrispin, and M. A. L. Bell, "A deep learning-based approach to identify *in vivo* catheter tips during photoacoustic-guided cardiac interventions," in *Photons Plus Ultrasound: Imaging and Sensing 2019*, vol. 10878. SPIE, 2019, pp. 454–460.

[23] E. M. A. Anas, H. K. Zhang, J. Kang, and E. Boctor, "Enabling fast and high quality LED photoacoustic imaging: A recurrent neural networks based approach," *Biomed. Opt. Express*, vol. 9, no. 8, p. 3852, 2018.

[24] A. Hariri, A. Hariri, K. Alipour, K. Alipour, Y. Mantri, J. P. Schulze, J. P. Schulze, J. V. Jokerst, J. V. Jokerst, and J. V. Jokerst, "Deep learning improves contrast in low-fluence photoacoustic imaging," *Biomed. Opt. Express, BOE*, vol. 11, no. 6, pp. 3360–3373, 2020.

[25] F. Kalloor Joseph, A. Arora, P. Kancharla, M. Kuniyil Ajith Singh, W. Steenbergen, and S. S. Channappaya, "Generative adversarial network-based photoacoustic image reconstruction from bandlimited and limited-view data," in *Photons Plus Ultrasound: Imaging and Sensing 2021*, A. A. Oraevsky and L. V. Wang, Eds. Online Only, United States: SPIE, 2021, p. 54.

[26] B. E. Treeby and B. T. Cox, "K-Wave: MATLAB toolbox for the simulation and reconstruction of photoacoustic wave fields," *JBO*, vol. 15, no. 2, p. 021314, 2010.

[27] L. Wang, S. L. Jacques, and L. Zheng, "MCML—Monte Carlo modeling of light transport in multi-layered tissues," *Computer Methods and Programs in Biomedicine*, vol. 47, no. 2, pp. 131–146, 1995.

[28] S. L. Jacques, "Optical properties of biological tissues: A review," *Phys. Med. Biol.*, vol. 58, no. 11, pp. R37–R61, 2013.

[29] M. Jaeger, S. Schüpbach, A. Gertsch, M. Kitz, and M. Frenz, "Fourier reconstruction in optoacoustic imaging using truncated regularized inverse k-space interpolation," *Inverse Problems*, vol. 23, no. 6, pp. S51–S63, 2007.

[30] H. J. van Staveren, C. J. M. Moes, J. van Marie, S. A. Prahl, and M. J. C. van Gemert, "Light scattering in Intralipid-10% in the wavelength range of 400–1100 nm," *Appl. Opt., AO*, vol. 30, no. 31, pp. 4507–4514, 1991.

[31] M. K. A. Singh, *LED-Based Photoacoustic Imaging: From Bench to Bedside*. Springer Nature, 2020.

[32] P. Arbeláez, M. Maire, C. Fowlkes, and J. Malik, "Contour Detection and Hierarchical Image Segmentation," *IEEE Transactions on Pattern Analysis and Machine Intelligence*, vol. 33, no. 5, pp. 898–916, 2011.

[33] B. C. Russell, A. Torralba, K. P. Murphy, and W. T. Freeman, "LabelMe: A Database and Web-Based Tool for Image Annotation," *Int J Comput Vis*, vol. 77, no. 1, pp. 157–173, 2008.

[34] R. O. Duda and P. E. Hart, "Use of the Hough transformation to detect lines and curves in pictures," *Commun. ACM*, vol. 15, no. 1, pp. 11–15, 1972.

[35] W. Xia, S. Noimark, S. Ourselin, S. J. West, M. C. Finlay, A. L. David, and A. E. Desjardins, "Ultrasonic Needle Tracking with a Fibre-Optic Ultrasound Transmitter for Guidance of Minimally Invasive Fetal Surgery," in *Medical Image Computing and Computer-Assisted Intervention - MICCAI 2017*, M. Descoteaux, L. Maier-Hein, P. Jannin, D. L. Collins, and S. Duchesne, Eds. Cham: Springer International Publishing, 2017, vol. 10434, pp. 637–645.

[36] W. Xia, S. Noimark, E. Maneas, N. M. Brown, M. K. A. Singh, S. Ourselin, S. J. West, and A. E. Desjardins, "Enhancing photoacoustic visualization of medical devices with elastomeric nanocomposite coatings," in *Photons Plus Ultrasound: Imaging and Sensing 2019*, vol. 10878. International Society for Optics and Photonics, 2019, p. 108783G.

Supplementary materials for “Improving needle visibility in LED-based photoacoustic imaging using deep learning with semi-synthetic datasets”

Mengjie Shi, Tianrui Zhao, Simeon J. West, Adrien E. Desjardins, Tom Vercauteren, and Wenfeng Xia

1 Receiver Operation Characteristic (ROC) Curves

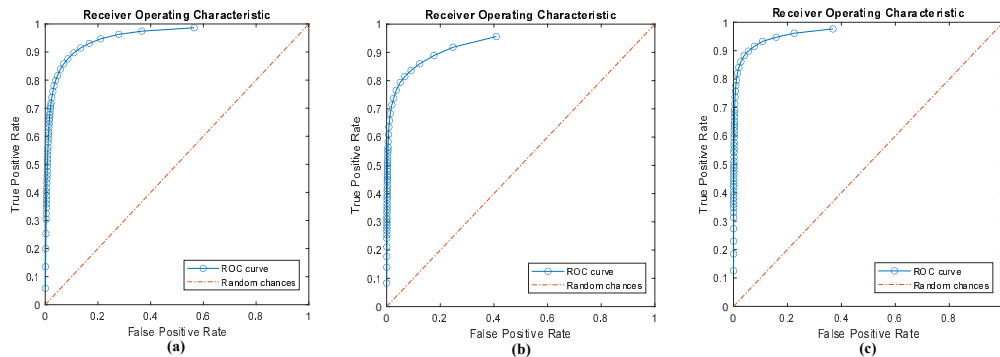


Figure 1: Receiver operation characteristic (ROC) curves for (a) a blood-vessel-mimicking phantom, (b) pork joint *ex vivo* tissue, and (c) *in vivo* measurements using human fingers.

Receiver operation characteristic (ROC) curves in Fig. 1 and Fig. 2 were used for finding optimised classification thresholds in conventional reconstructions. True positive rate (TPR) and False positive rate (FPR) were plotted for each decision threshold ranging from 1 to 250 with an increment of 5 in grayscale images. For each experiment, the cut-off point on each curve was chosen as the furthest point from the line that represents the random chances as a result of balancing TPR and FPR.

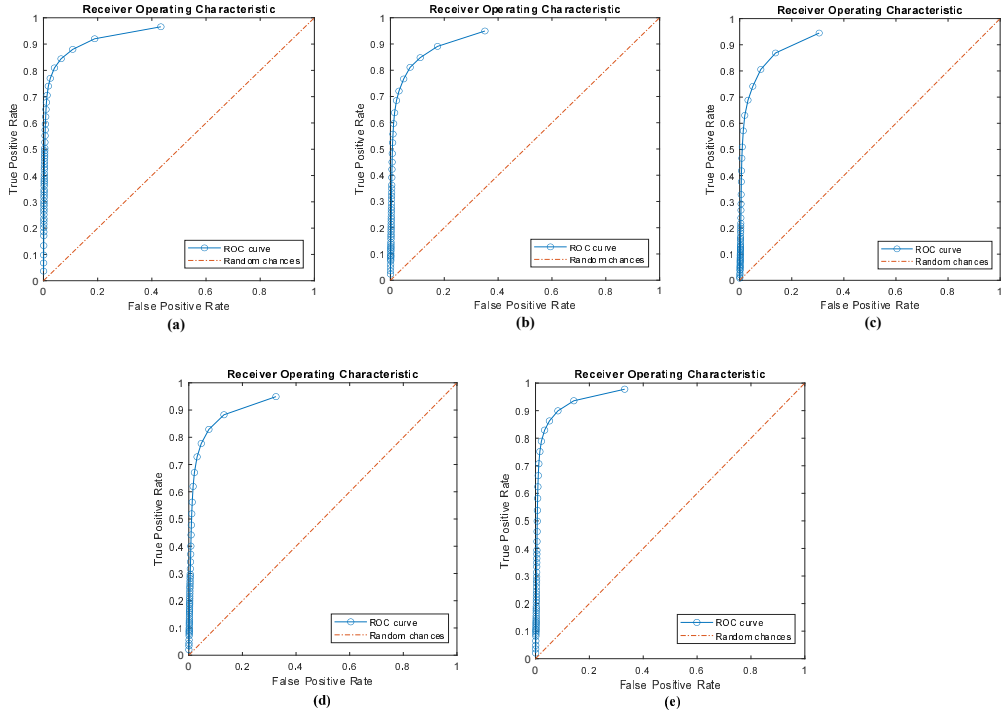


Figure 2: Receiver operation characteristic (ROC) curves for different needle diameters: (a) 16G (b) 18G (c) 20G (d) 25G (e) 30G.

2 Impact of Needle Diameters

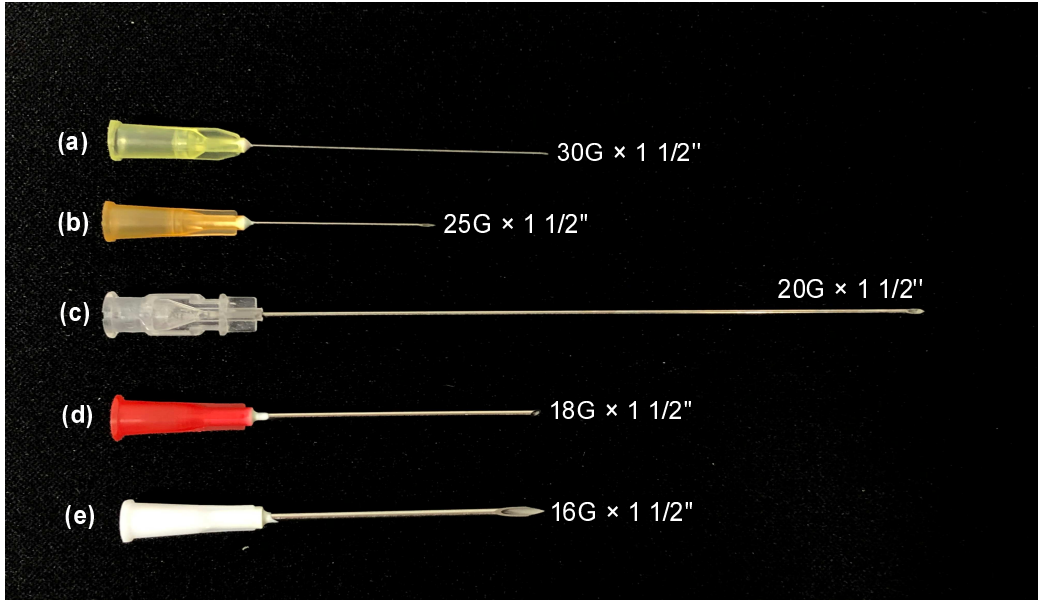


Figure 3: Photograph of metallic needles with different diameters: (a) 16G (b) 18G (c) 20G (d) 25G (e) 30G.

Table 1: Quantitative evaluation of the performance of trained neural network using with respect to needles with different diameters using measurements on ex vivo tissue

Metrics	16G		18G		20G		25G		30G	
	CR ^a	U-Net Enhancement								
SNR	8.2308	43.4552	6.5324	49.1835	4.3885	37.1594	5.3055	34.0216	7.0228	45.0623
IoU	4.6%	35.6%	6.7%	36.2%	8.1%	30.3%	5.2%	29.9%	10.9%	36.4%
PPV	4.7%	72.2%	6.8%	79.5%	8.4%	75.2%	5.1%	73.3%	11.2%	80.3%
TPR	87.9%	41.4%	89.1%	39.8%	86.9%	33.5%	88.3%	33.7%	89.9%	39.8%
ASD	3.2632E+05	1605.7700	3.5092E+05	1150.2305	3.6730E+05	1096.9343	3.3731E+05	1075.9791	2.4260E+05	1039.6999

^aConventional Reconstruction

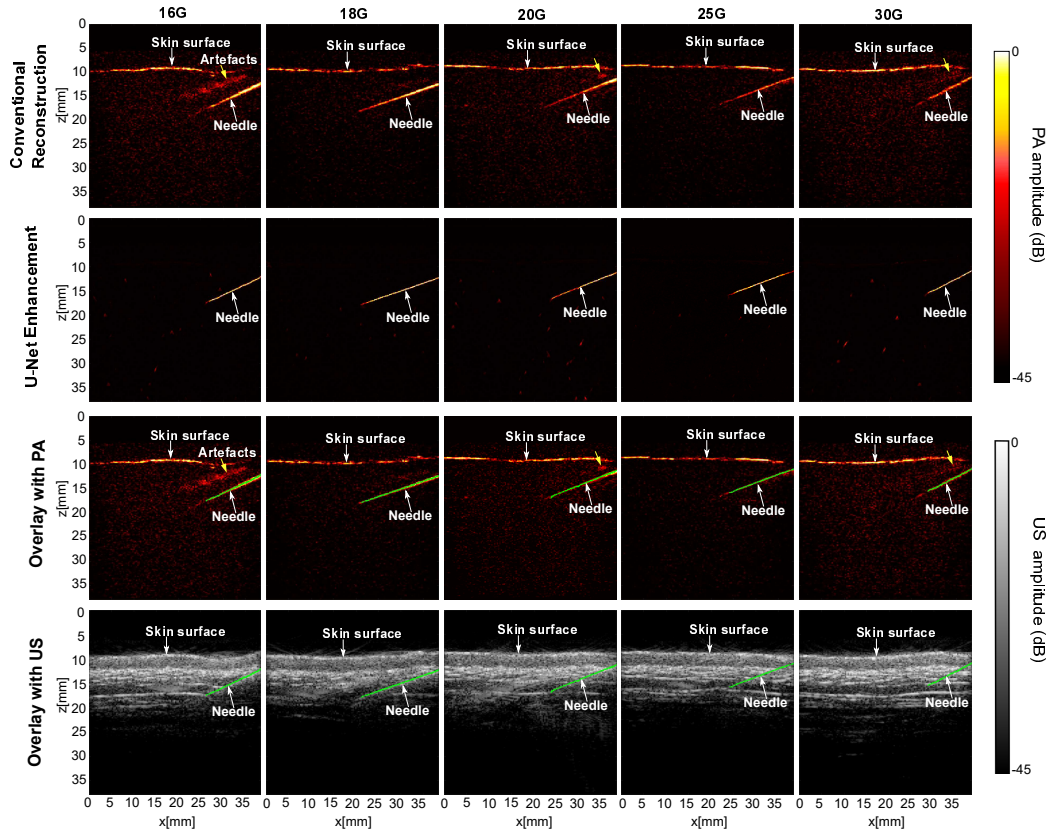


Figure 4: Photoacoustic imaging with needle insertions into pork joint *ex vivo* tissue for needles with different diameters with conventional reconstruction, U-Net enhancement, and U-Net enhancement post-processing.